If AFM can be used to measure absolute values of the Young’s modulus of nanocomposite materials down to the nanoscale?

Journal:	*Nanoscale*
Manuscript ID	NR-ART-03-2020-002314
Article Type:	Paper
Date Submitted by the Author:	23-Mar-2020
Complete List of Authors:	Liu, Yuke; Tufts University; Guangzhou Institute of Geochemistry, CAS Sokolov, Igor; Tufts University Dokukin, Maxim; Tufts University Xiong, Yongqiang; Guangzhou Institute of Geochemistry, CAS, Peng, Ping'an; Guangzhou Institute of Geochemistry,

Can AFM be used to measure absolute values of the Young's modulus of nanocomposite materials down to the nanoscale?

Received 00th January 2020,
Accepted 00th January 2020

DOI: 10.1039/x0xx00000x

Y. Liu[a,b,f], I. Sokolov[a,c,d, *], M.E. Dokukin[a,e], Y. Xiong[b], P. Peng[b]

At present, a technique potentially capable of measuring values of the Young's modulus at the nanoscale is atomic force microscopy (AFM) working in the indentation mode. However, the question if AFM indentation data can be translated into absolute values of the modulus is not well-studied as yet, in particular, for the most interesting case of stiff nanocomposite materials. Here we investigate this question. A special sample of nanocomposite material, shale rock, was used, which is relatively homogeneous at the multi-micron scale. Two AFM modes, Force-Volume and PeakForce QNM were used in this study. The nanoindenter technique was used as a control benchmark for the measurement of the effective Young's modulus of the shale sample. The indentation rate was carefully controlled. To ensure the self-consistency of the mechanical model used to analyze AFM data, the model was modified to take into account the presence of the surface roughness. We found an excellent agreement between the average values of the effective Young's modulus calculated within AFM and the nanoindenter benchmark method. At the same time, the softest and hardest areas of the sample were seen only with AFM.

Introduction

Knowledge of the mechanical properties of materials at the nanoscale is important for the development of novel materials [1], for understanding the behavior and function of biological systems, for the study of nanoscale objects [2-4], cells [5]. Mechanics of biological cells have also been used in the study physics of various diseases [6-8] and even aging [9, 10].

At present, the nanoindenter [11] and atomic force microscopy (AFM) are the methods to directly probe mechanics at the nanoscale. Both techniques utilize a fine probe, which indents the sample surface while recording the force-indentation curves. Mechanical properties of the sample material (the Young's modulus and hardness) can be extracted by analysing the recorded force-indentation curves. AFM, being initially developed as an imaging technique, can operate with a much smaller indentation force range. However, the load system of AFM, which is based on a cantilever bending, is not an ideal indentation system. The AFM probe cannot develop a straight vertical indentation for the entire load range. Therefore, to use AFM for an accurate nanoindentation experiment, special care of the force range, and the cantilever stiffness and geometry are required [12]. On the other hand, the AFM nanoindentation allows considering the force of adhesion between the indenting probe and sample, which is important when using a small load force. As a result, even a small indentation allows to extract the elastic modulus in a rather precise quantitative manner [12]. Nanoindenter utilizes Pharr-Oliver model [11], which does not take into account adhesion. Therefore, reliable measurements of the elastic modulus when using the nanoindenter can only be done starting from a sufficiently large indentation, when the adhesion force is negligible compared to the load force. Because the spatial resolution of the mapping of mechanical properties using these techniques is mainly defined by the area of contact between the indenting probe and sample surface, the lateral resolution of mechanical maps obtained with the nanoindenter method is substantially lower compared to AFM.

When measuring rigid materials, the nanoindenter is typically a more accurate method compared to AFM because it requires larger forces, which are hard to obtain with AFM. Secondly, since the nanoindenter works with large indentations, the sample preparation is easier for the nanoindenter because it does not require delicate high-quality polishing of the sample surface, which is a prerequisite for almost all AFM tests[13].

AFM is preferable when studying soft materials because it can operate with smaller force (the nanoindenter approach can still be used for such materials, but the area of contact is too large to be called "nano"). The force-volume mode [14-16] and recently introduced sub-resonance tapping modes can provide the nanoscale quantitative mapping of mechanical properties at a high resolution [17]. The force-volume mode has been traditionally used for a quantitative study of sample mechanics. A sub-resonance tapping, for example, PeakForce QMN is a newer mode, which can mostly be used for obtaining images of a relative rather than the absolute distribution of mechanical properties of samples [12 17]. The AFM technique has been widely used to characterize the nanomechanical properties of biological materials [18-20], polymers [12, 21, 22], cement minerals [23], and even shale [24-26].

The nanoindenter technique was proven to be rather precise, whereas the AFM method is yet in the process of establishing AFM as a robust quantitative technique. A direct experimental comparison of the indenter and AFM techniques, as well as the validation of the results obtained with different AFM modes, are the ways to demonstrate the quantitative and robust nature of the AFM measurements. Such comparison has been previously done for only relatively soft and homogeneous polymers by using the AFM HarmoniX and PeakForce QNM modes [16]. One of the conclusions of that work was the need to

---

[a] Department of Mechanical Engineering, Tufts University, Medford, MA, USA.
[b] Guangzhou Institute of Geochemistry, Chinese Academy of Sciences, Guangzhou, China.
[c] Department of Biomedical Engineering, Tufts University, Medford, MA, USA.
[d] Department of Physics, Tufts University, Medford, MA, USA
[e] Sarov Physics and Technology Institute, National Research Nuclear University MEPhI, Sarov, Russian Federation
[f] Guangzhou Marine Geological Survey, China Geological Survey, Guangzhou, China
* Corresponding author: igor.sokolov@tufts.edu

use a relatively dull AFM probe. It was in agreement with ref.[12], which demonstrated that a commercially sharp AFM probe inevitably led to a nonlinear stress-strain response of the sample material. However, no comparative research has been done on heterogeneous and relatively rigid composites like shales so far. Due to the complexity of the AFM setup and higher force sensitivity, such a comparison is paramount to demonstrate the accuracy and lack of artifacts in the AFM indentation approach.

Here we demonstrate that AFM is a robust and quantitative method of measurements of nanocomposite materials exampled by a special shale rock sample. This particular sample is sufficiently homogeneous at the multi-micron scale. This homogeneity is needed to compare the measurements of the nanoindenter and AFM techniques because it is rather hard to colocalize precisely the areas of the measurements for both techniques. This homogeneity is verified by measuring the mechanical property of the sample surface at multiple multi-micron areas. It was further confirmed by complementary SEM elemental analysis and Raman confocal spectroscopy of the sample to demonstrate a relatively homogeneous distribution of the organic phase in this shale sample (the contact with the softest, organic phase decreases the heterogeneity of mechanical response of composite material). At the same time, the sample, being nanocomposite, is definitely heterogeneous at the nanoscale. So we can speak only about an effective Young's modulus.

The effective Young's modulus of the shale sample is measured using the nanoindenter method and both AFM modes described above, PeakForce QNM and force-volume. The comparison is done for a large range of unloading rates to match substantially different rates of the nanoindenter and AFM. The self-consistency of the used mechanical models has to be verified to obtain the absolute values of the effective Young's modulus. It was done by monitoring the modulus independence of the indentation depth. To obtain the modulus from the AFM measurements, we present a theoretical method that takes into account an inevitable surface roughness of nanocomposite samples.

The choice of shale rocks was justified not only by its mechanical properties described above but also because of its practical importance. Knowledge of mechanics of shale rocks is essential to success in many aspects of the exploration, extraction, and recovery of oil and gas [27, 28]. One of the most important tasks in the development of unconventional reservoirs hosted by organic-rich shales is an accurate prediction of the mechanical integrity of the reservoirs [29]. However, the prediction of mechanical properties of organic-rich shales is intricate due to their complicated chemistry, heterogeneous nanostructure, and multiscale mechanical performances. The high complexity nature of shales requires advanced and innovative experimental and theoretical tools for understanding the role of different constituents (i.e., organic and inorganic components) in the chemo-mechanical properties at multiple scales. Macroscopic measurements of shale strength and/or stiffness in the field and laboratory have typically been conducted using unconfined compression tests[30], standard triaxial tests [31], polyaxial tests [32], or acoustic techniques [33], which have problems of precision, large discrepancies, and low repeatability [34]. These problems can lead to a significant error in the measured mechanical properties [35].

The organic component is typically well distributed in the shale body down to the nanoscale, which makes shales a nanocomposite [36-39]. Mechanics of nanocomposites can be mainly defined by the mechanical properties of the interface between different phases. The properties of the interface cannot be derived from the macroscopic mechanical properties of the phases measured separately. Therefore, the direct measurements of the distribution of mechanical properties of shales at macroscale is useful for understanding the elasticity and rheology of organic-rich shale in the macro scale.

Here we demonstrate that the AFM technique can be used the measure the absolute values of the effective Young's modulus of nanocomposite materials down to the nanoscale. An agreement was observed between the established quantitative technique, the nanoindenter, and the AFM indentation modes. Specifically, we observed an excellent agreement between the average values of the effective Young's modulus obtained with the nanoindenter and AFM techniques. At the same time, the softest and hardest areas of the sample were seen only with AFM due to its substantially higher lateral resolution. A novel method of the analysis of AFM indentation curves is presented, which takes into account the presence of the surface roughness.

Experimental section

Materials

A pure organic matter sample (solid bitumen) and a composite material (shale) were used in this study. A solid bitumen sample was collected from Shuiquan Formation, eastern Tarim Basin, China, which has a TOC of ~98% and a vitrinite reflectance (%Ro) of 3.68±0.02 % [40]. The shale sample was collected from a depth of 1618 meters in drilling well of the lower Silurian Longmaxi Formation in Sichuan Basin, southwestern China. The shale sample has a TOC of 5.05% and mineral composition of quartz (48.6%), feldspar (9.1%), carbonate (1.4%), pyrite (2.0%), and clays (38.9%).

Prior to the measurements, samples were prepared as follows. First, the samples were embedded in epoxy and then polished by mechanical polishing, followed by argon ion beam polishing. Sandpapers with different sizes of grit ranging from 1200 to 2000 were used to polish the sample surface at the stage of mechanical polishing. Then aluminium oxide suspension polishing fluid (grain sizes of 2 µm and 0.25 µm) was utilized. Subsequently, the samples were exposed to argon ion milling using a Cross Section Polisher (JEOL Inc.). Planar milling type with a 3° inclination was used, and the milling was performed under 5 kV for 0.5 h (see the discussion of possible alteration of the sample surface due to ion milling in the Supplementary materials). The level of final roughness was measured by AFM PeakForce QNM mode with a standard commercial probe (ScanAsyst probes for imaging in air, Bruker, Inc.) The average surface root means square (RMS) roughness in an area of 10 μm ×10 μm^2 was found to be 4.3 ± 1.0 nm and 30.6 ± 4.2 nm for solid bitumen and shale, respectively.

Methods

Nanoindenter method

The nanoindentation experiments were performed by means of an iNano Nanoindenter (Nanomechanics Inc.). A diamond Berkovich probe was used. The dependence of the probe area on the probe height was measured by using indenting a fused quartz standard [41]. All experiments were performed at room temperature (22 − 24 ℃) and relative humidity of 40 − 60%. The cyclic rate loading method was adopted for different unload speeds. A three-step procedure was applied as (1) increase the load at a constant strain rate of 0.5 s^{-1} to the maximum force set; (2) hold the maximum load for 2 s; (3) linearly decrease the load to zero within a predefined time (of several seconds). The creep drift in each indentation experiment was ≤ 0.2 nm/s.

The reduced Young's modulus was calculated from the unloading part of load−indentation curves (40% to 95% of the maximum load) using the Oliver−Pharr method [41]. These specific percentages of the maximum load were chosen because the modulus is reasonably independent of the indentation depth within these limits (described later in detail). By using the contact measured stiffness, S (=dP/dh, where P is the load and h is the indentation depth), and the projected contact area A, one can find the reduced indentation modulus, E_r, as follows

$$E_r = s\frac{\sqrt{\pi}}{2\sqrt{A}} \ . \tag{1}$$

The Young's modulus of the sample can now be found using the following equation:

$$\frac{1}{E_r} = \frac{(1-v^2)}{E} + \frac{(1-v_i{}^2)}{E_i} \ , \tag{2}$$

where E and v are the Young's modulus and Poisson's ratio of the sample (v=0.3 is used in this study [13, 42]; the specific value of the Poisson's ratio does not influence the comparison of three methods used in this work), E_i = 1140 GPa and v_i=0.07 are taken for the diamond indenter, Berkovich probe, used in this study [43].

Since the model described above doesn't take into account the probe sample adhesion, one needs to work with a relatively large force (much larger than the adhesion force) to ignore the adhesion. In addition, the indentation should not be too small on both shale and bitumen samples to eliminate possible non-linear deformation for small indentation depths [12] as well as small but still existing roughness of the sample surface. One of the simple and robust methods to find the appropriate values of the load force (contact area and indentation depth) is the use of the strong linearity principle [12, 44, 45]. This principle implies that the derived modulus should be independent of the indentation depth/load force. To do it, we changed the maximum indentation depth from 200 nm to 1500 nm (while the unloading time of 2 s was utilized for this part of the study).

To demonstrate the important steps of the method, we show a typical force-indentation curve for the shale sample, Fig. 1a. The difference between load and unload force curves are due to the creep relaxation of the sample and plastic deformation. The moduli are calculated with formulas (1) and (2) using the method of [41]. Following the measurement protocol, the modulus was investigated at different indentation depths. The modules for each indentation depth was measured for an array of 15×15 indents. To avoid indenting sample areas that were previously deformed, the spacing between the indents was 10 μm (7-10 times the sizes of the indentation depth). As was demonstrated in [46], such close proximity of indentation brings a negligible error compared to the variation of the obtained moduli. The results are shown in figure Fig. 1b. One can see the presence of depth independent plateau starting from 500-700 nm of indentation depth.

The modulus of the sample is given by the value of the plateau according to the nanoindenter protocol. Hereafter, the modulus of shale is measured using the indentation depth of 1000 nm (under an applied force of 20 mN).

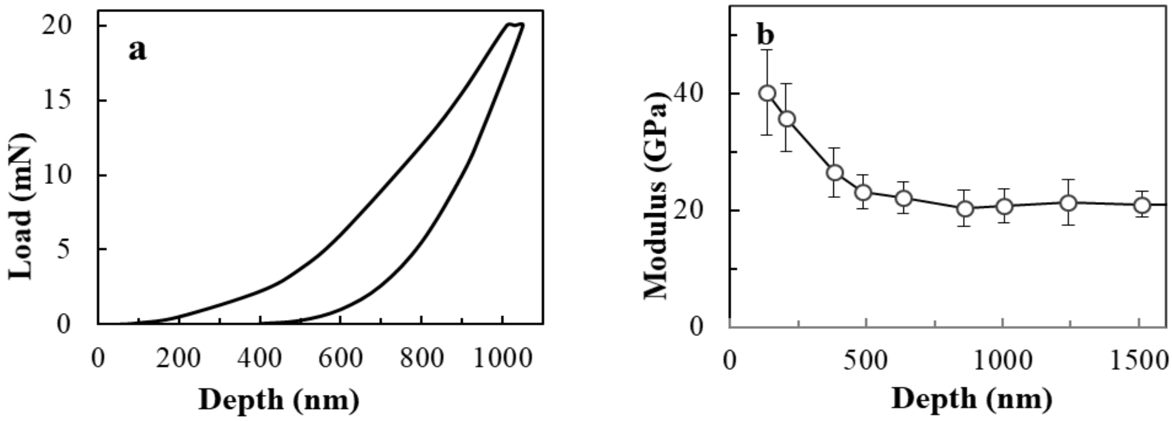

Fig. 1. Nanoindenter examples of (a) load-depth of shale with the applied force of 20 mN and unloading rate of 200 nm/s; both load and unload force curves are shown, (b) the Young's modulus (E) of the shale sample as a function of the maximum indentation depth (each dot represents the average modulus value of 15 × 15 values (150×150 μm^2), with one standard deviation error bar).

Atomic Force Microscopy

Dimension Icon (Bruker Nano/Veeco, Inc., CA) AFM with Nanoscope V controller and Nanoscope 8.15 software were used to acquire both force−indentation curves and surface topographic maps. A regular RTESP AFM probe (Bruker Nano/Veeco, Inc., hereafter, sharp probe) was used to characterize the sample roughness. The obtained geometry (height) maps were processed through the SPIP 5.1.11 (Image Metrology A/S) and NanoScope Analysis v.1.5 (Bruker, Inc.) to find the sample roughness and to identify relatively flat surface areas.

Similar to the nanoindenter, the Young's modulus may depend on the indentation force/indentation depth. As was shown, e.g., in [12], a sharp AFM probe cannot be used for reliable quantitative measurements of mechanics because of the nonlinearity of stress-strain relation, which occurs for the common sharp AFM probes. A similar problem was recently demonstrated for soft materials like cells [47, 48]. To avoid this problem, a parabolic "dull" probe (NanoScience Solutions, Inc.) was used in this study for modulus measurement. The geometry of the dull probe was found by imaging a tip-check sample (Budget Sensor, Inc.). The obtained probe used in this work has a spherical shape of the apex with a radius of 320 ± 10 nm (Fig. 2). The spring constant of the AFM cantilever was chosen to produce sufficient indentation on the hard materials of study. It was difficult to use the standard thermal tuning on such cantilever (the nominal spring constant ~200N/m). Therefore, the spring constant was measured by using bitumen as the reference material [49]. The Young's modulus of bitumen was taken from the nanoindenter measurements (9.0 GPa), which was in agreement with the previously reported values [26]. The found spring constant of the AFM cantilever was 215±10 N/m. Before each test, the sensitivity of the AFM photodetector (deflection sensitivity) was measured by using a clean sapphire standard. It is important to note that the sensitivity was measured for the force range used to calculate the modules, see the supplementary materials for detail.

Two AFM indentation modes, force-volume and PeakForce QNM (a sub-resonance tapping mode by Bruker, Inc) were used in this study. Because of the existence of a viscous component of the samples, it is important to match the indentation unload rates when comparing results obtained by the different techniques. We used a range of the unloading rates for both of the AFM modes. To avoid artifacts of non-flat geometry that are not taken into account in the existing models, we used the data collected on relatively flat regions of the sample for both PeakForce QMN and Force-volume modes (the topography can simultaneously be measured in both modes). Only the modulus from the areas with height gradient less than 5 degrees was taken into account (such areas were automatically identified with the help of SPIP software, see the Supplementary materials for details of the algorithm).

AFM Force-Volume mode for measuring sample mechanics

This mode is one of the oldest AFM modes, which can be used to study the mechanical properties of samples [15]. The disadvantage of this mode is a relatively slow data acquisition. Being rather accurate for quantitative analysis, this model is not used for imaging (high-resolution mapping of the sample surface). The imaging of mechanical properties is typically done with sub-resonance tapping, PeakForce QNM (see, the next section for detail). An advantage of the force-volume mode is the ability to use a broad range of indentation speeds/rates. This is important because the elastic modulus is generally rate-dependent. To be able to compare all three methods used in this work, the force−indentation curves were recorded at various vertical unloading speeds from 200 nm/s (0.5 Hz ramp rate and 200 nm Z ramp size) to 117,000 nm/s (3 Hz ramp rate and 4.5 μm Z ramp size), with a maximum load force of 8 μN and an average indent depth of 5 nm [50]. This indentation speeds cover the unloading rates of nanoindenter (100-1000 nm/s) and PeakForce QNM (25,000 nm/s and 50,000 nm/s, described later in detail).

The Young's modulus on the samples was calculated as follows. The reduced modulus $\boldsymbol{E_r}$ was first calculated by fitting the retract curve with the DMT model:

$$\boldsymbol{F = \frac{4}{3}E_r\sqrt{R\delta^3} + F_{adh}} \tag{3}$$

where *F* is the load force, *R* is the curvature radius of the AFM probe, $\boldsymbol{\delta}$ is the indentation depth, and F_{adh} is the adhesion

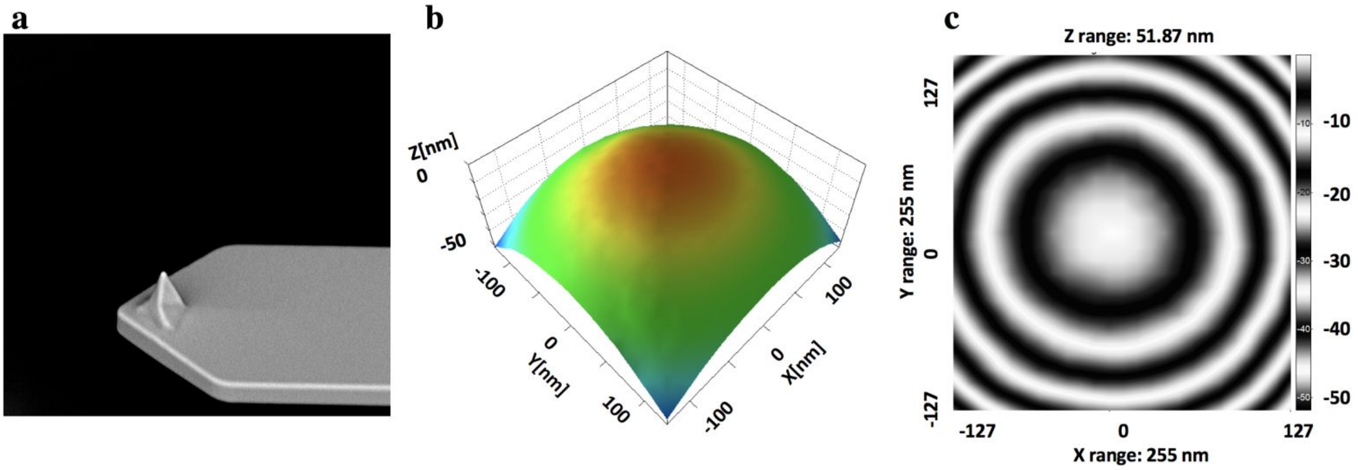

Fig. 2. (a) SEM image of the dull AFM probe used in the present work; (b,c) the geometry of the probe apex obtained through the imaging of the tip-check sample.

force (pull-off) between the AFM probe and sample. The Young's modulus E is then found using equation (2), in which E_i and v_i are the Young's modulus and Poisson ratio of the AFM probe (the reduced modulus of the probe $E_r = 120GPa$; this value was obtained by measuring deformation of the probe with respect to two calibration samples, see the Supplementary materials for detail). This particular model was chosen using the same logic based on the Magnus parameter, as described in [12, 16].

The contact diameter d for the DMT model can be calculated through the following equation:

$$\boldsymbol{d} = \boldsymbol{2}\sqrt[3]{\frac{\boldsymbol{3(F_{Lmax} + F_{adh})R}}{\boldsymbol{4E_r}}} + \boldsymbol{F_{adh}}. \tag{4}$$

The contact diameter is useful to know to calculate the minimum distance between neighbouring indentations to avoid either the redundant measurements of essentially the same contact (when there is no plastic deformation) or dealing with a disturbed sample surface (if there is plastic deformation). Thus, the distance between each touchpoint on the surface studied with the force-volume mode in this work is larger than the contact diameter.

To demonstrate the important steps of the method, we present a typical force indentation curve for the sample of interest. Fig. 3a shows typical force-indentation curves for the shale and bitumen surfaces. Both the trace and retrace (load and unload) curves are shown. The differences between these two curves are explained by irreversible (plastic) deformation and viscoelastic response of the sample. It should be noted a substantially different behaviour of the force curve for forces higher than 8 μN. This is explained by the lateral motion of the apex of the AFM probe during the indentation, which is a known problem of AFM nanoindentation (it depends on the probe geometry; this effect is substantially stronger when a sharp AFM probe is used). Here it implies that 8 μN is the maximum force indentation that can be used in the present setup.

The second important part is taking into account the surface roughness of the samples inevitable for non-crystalline surfaces. Because of the presence of surface roughness, the initial part of the indentation force curve cannot be used to define the modulus. Although the sample preparation was done rather carefully, the residual roughness still exists. The analysis of AFM images of the shale sample surface (e.g., Fig.S1) shows a typical peak-to-valley roughness of the order of 1 nm at the scale of the AFM probe contact (about 80 nm, see the Results and discussion section for detail). The roughness cannot be simply ignored by considering only higher forces. This has been demonstrated for a rather similar contact problem, the indentation of biological cells which are covered with a highly nonlinear pericellular coat layer. This problem was resolved within the so-called brush model [51-53]. It essentially requires to do the fitting of small portions of the force indentation curve by treating both modulus and the position of the bulk material as unknown parameters. The logic behind it is that the roughness asperities (being less stiff compared to the continuum) will be squeezed by the indenter till their stiffness is equal to the stiffness of the bulk material. The larger forces will deform the material bulk. If one works in a linear stress-strain regime, it should result in the independence of the modulus of the load force. This is the necessary requirement of the self-consistency of the DMT model.

Thus, one needs to identify the range of forces, in which the used DMT model is self-consistent, i.e., the modulus is independent of the indentation depth. In the particular example of force-indentation curves for solid bitumen and shale shown in Fig. 3a, the plateau in the modulus depth/force dependence corresponds to the load force of 5-7.5 μN, as shown in Fig.3b. This corresponds to a top part of the retrace curve (60% to 90% of the maximum load). For smaller forces/indentation, one can see smaller values of the modulus, which is plausible because it requires less force to deform roughness asperities.

AFM Peak-Force QNM mode for measuring sample mechanics

Peak-Force QNM sub-resonance tapping was the second indentation AFM technique used to measure the shale mechanics. The same size (10 × 10 μm^2) and in the same position on the sample surface were measured right after finishing each force-volume scan. This was allowed because the plastic deformation was not observed in the force-volume scans (presumably due to a relatively small indentation force). It is confirmed by the overlap of the load and unload force curves (at the force range used to calculate the Young's modulus), and no creep observed (both load and unload force curves start at the same point). It should be noted that if we had any plastic deformation, it could be easily seen directly in the scans of PeakForce QNM because it is an imaging mode and provides much higher spatial resolution than the force-volume one. The digital (pixel) resolution was substantially higher (128 × 128 pixels) compared to the one obtained in the force-volume mode. Because the same exact surface area and AFM probe were used for both force-volume and PeakForce QNM modes, the same load force (8 μN) and fitting force range (5 to 8 μN) were used to obtain the Young's modulus (the plateau value) in PeakForce QNM. The lateral scanning rate was 0.5 Hz. The vertical oscillation/ramping of the probe was set to 1 kHz with an amplitude of 65 nm and 200 nm (corresponding to approaching/retract speed of 25,000 nm/s and 50,000 nm/s, respectively), which are within the speed range in the force-volume mode. Lower amplitudes, and consequently, smaller speeds were impossible to reliably control due to a large probe sample adhesion. The deflection sensitivity was measured similarly to the force-volume mode.

Electron and Raman microscopy

A scanning electron microscope, SEM (Phenom, FEI) with EDS option for elemental analysis was used. 10 keV accelerating voltage was used for the imaging and 15keV for the EDS analysis. The polished samples were imaged as is, without any additional treatment or coating.

Raman confocal imaging was done using a confocal Raman microscope Alpha 300 (WITec, Inc.). A blue laser (488 nm) was

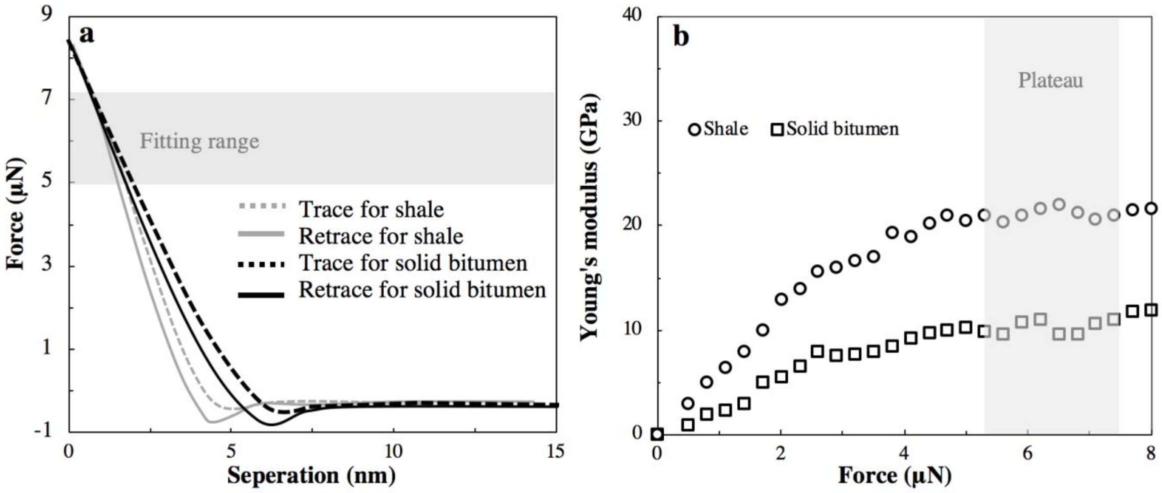

Fig. 3. Examples of force-indentation curves (a) and modulus-force curves (b) of shale and bitumen samples collected using the force-volume mode (0.5 Hz ramp rate and 200 nm Z ramp size). The grey region in (a) is the fitting force range with eq. 3, the DMT model, and (b) is the modulus plateau, which corresponds to the fitting force range.

used for both shale and solid bitumen samples. The power of the laser was adjusted to avoid any possible damage to the sample during the imaging.

Results and discussion

The effective Young's modulus was found using the AFM indentation method, which was described in the previous section, applied to multiple points on the sample surface. Specifically, a force-volume map with a size of 10 ×10 μm^2 and a resolution of 32 × 32 pixels (one force–separation curve was recorded at each pixel) under an unloading speed of ranging from 200 to 117000 nm/s were obtained. Sequentially, PeakForce QNM images of the modulus were recorded with a resolution of 128x128 pixels on the same area with the peak force corresponding to the plateau of the modulus. The unload speed was estimated to be 25,000 and 50,000 nm/s (25,000 nm/s unload speed was the minimum possible for PeakForce QMN, which gave a reasonably good quality of data).

It is worth noting that the distance between the individual pixels in the maps of the modulus is ~80 nm (the length 10 μm divided by 128 pixels) for PeakForce QNM and 312 nm (the length 10 μm divided by 32 pixels) for force-volume mode. These values are larger or similar to the estimation of the area of contact (diameter of ~80 nm) between the probe and sample using Eq (4). This allows us to avoid oversampling during the measurements. Furthermore, these distances seem to be sufficiently large to avoid the concern of alteration of the sample by the AFM probe because the AFM nanoindentation used here works with forces within the linearity limit (< 8 µN). The distance between the indents is a concern in the nanoindenter technique [46] because the nanoindenter probe deforms the sample surface well beyond the linearity limit.

Fig. 4 shows a representative data for one of such areas of the shale sample. The unload rates were chosen to give the most accurate measurements for the force volume (200 nm/s) and PeakForce QNM (25,000 nm/s) modes. The topography and modulus maps, as well as the histogram of the modulus values are presented. The white areas on the distribution of the modulus are the areas with a large height gradient of topography (higher than 5°). The modulus was not calculated in those areas because of the absence of the corresponding model.

To demonstrate that the results obtained on 10x10 μm^2 area shown in Fig.4 are representative of the mechanical properties of the entire sample, we repeat the AFM measurements for 10 different areas of the same size. The results are presented in figure 5b,c, in which all 10 histograms are shown. One can see that all histograms are very similar.

To verify the results obtained from the AFM indentation with the benchmark, the nanoindenter, we did similar measurements using the nanoindenter to demonstrate the homogeneity of mechanical properties of the shale sample. Specifically, we examined 10 different areas of 150×150 μm^2. These larger sizes were used to avoid the influence of neighbour indents as explained in the Method section. An array of 15×15 indents was measured using the maximum load force of 20 mN at an unloading speed of ~200 nm/s. The results are presented in figure 5a. One can see that the histograms of distribution of the Young's modulus are virtually the same for all 10 areas. The coefficient of variations (CV; shown in the figure) of the 10 histogram distribution curves for each method are much less than 1. For all the methods, the standard deviation of the modulus for one area is much greater than the standard deviation between averages of the modulus between the 10 different areas.

Force-volume (Fig. 5 b) and PeakForce QNM (Fig. 5 c) methods show the distributions, which are positively skewed compared to the nanoindenter one (Fig. 5 a). This can be explained by higher spatial and force resolution of AFM. Apparently, small rigid clusters, particles of the inorganic phase can be detected with AFM, but not with the nanoindenter. Those more rigid parts of the sample contribute to the distribution tails of high moduli in the AFM measurements. Similarly, AFM allows detecting softer (pure organic) parts of the sample compared to the nanoindentation method, thereby presenting the tail of the smaller moduli. This information is important for the evaluation of the mechanical integrity of nanocomposites.

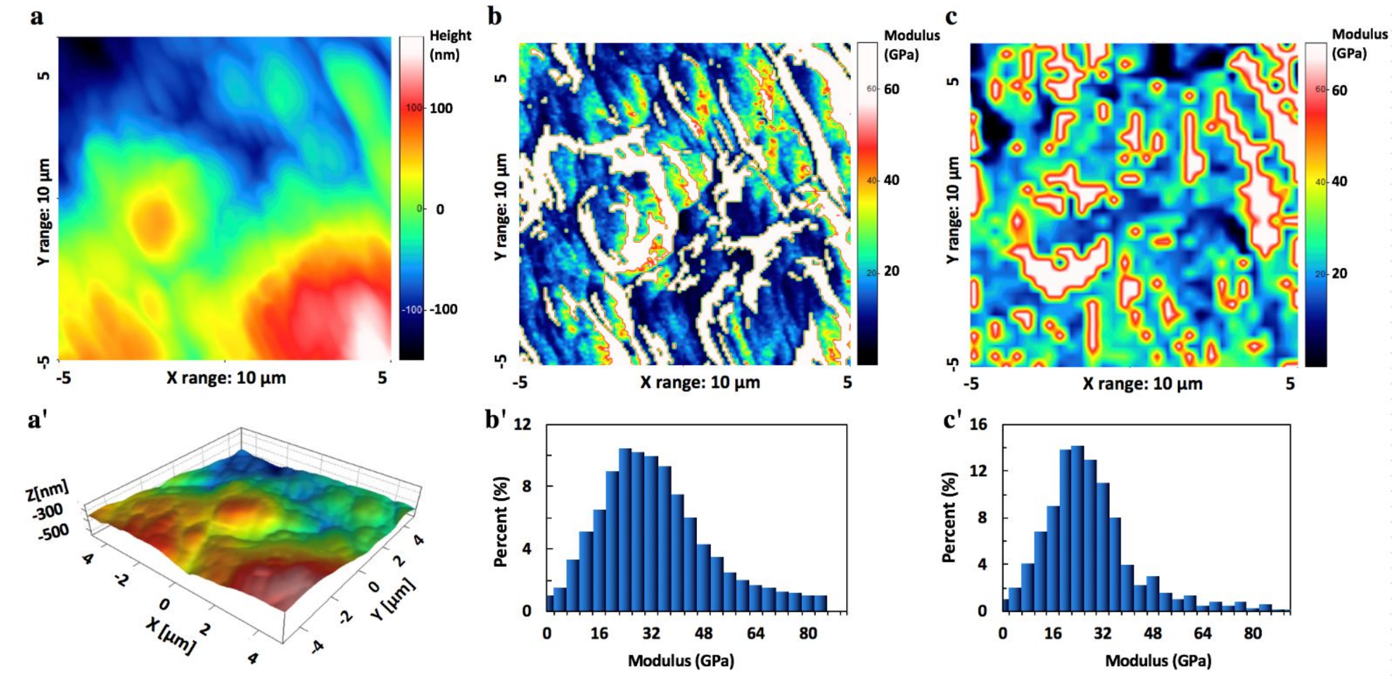

Fig. 4. Representative AFM scans obtained with the AFM Force-volume and PeakForce QNM modes applied to the same 10x10 μm^2 area. PeakForce QNM (unloading speed of 25,000 nm/s): (a) 2D and (a') 3D topography, (b) modulus map (the white areas correspond to excessively large height gradient (greater than 5 degrees), in which the modulus was not calculated) and (b') histogram of the modulus values shown on map (b). Force-Volume (unloading speed of 200 nm/s): (c) the map of the modulus values (the white areas correspond to the excessively high height gradient) and (c') the histogram of the modulus shown on map (c).

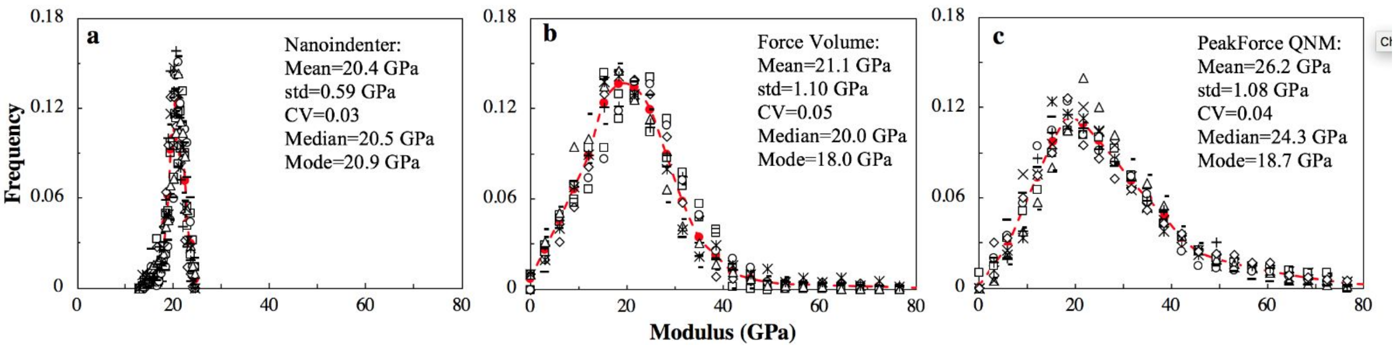

Fig. 5. Histograms of values of the Young's modulus measured on 10 different areas on the shale sample by using (a) nanoindenter with the maximum load force of 20 mN at an unloading speed of ~200 nm/s, (b) Force-volume with the maximum force of 8 μN at an unloading speed of 200 nm/s, (c) PeakForce QNM with the maximum force of 8 μN at an unloading speed of 200 nm/s. Each set of symbols represents one histogram of 15×15 indents for Nanoindenter, 32×32 indents for Force-Volume, and 128×128 indents for PeakForce QNM; the red dash-line represents the average distribution over of the 10 areas. The mean, std (standard deviation), and CV (coefficient variation) are calculated for the averages of 10 different areas; the median and mode are given for the averaged curve.

The observed average mechanical homogeneity of such a complex sample as shale is rather nontrivial. To understand the nature of the observed high homogeneity of the average mechanical of the shale rocks, it is worth noting that marine organic-rich shale is composed of brittle minerals (such as quartz, feldspar, calcite, and pyrite), clay, and organic matters. Most of the brittle minerals (such as quartz, feldspar, and carbonate) are in a dispersed or laminated form, pyrite is generally in spots form, organic phase, bitumen, are in the dispersed form (but in the laminated or banded form with the increase of organic matter abundance) in shale. At the same time, the organic component of shales is well distributed in the shale body down to the nanoscale [36-39], which implies that the mechanical properties of organic-rich shale rocks at the small-scale can be rather homogeneous despite the known structural heterogeneity [54].

To demonstrate that the organic phase is relatively homogeneously distributed in our samples, its distribution was investigated by SEM and Raman analysis. Backscattered SEM images of a 500x500 μm2 shale surface (shown in figure S2 of the supplementary materials) demonstrate a rather homogeneous distribution of contrast at the acceleration voltage of 5 kV. Images taken using such voltage show the material contrast near the surface. The same figure also shows an image taken of the same surface at 15 kV acceleration voltage, which probes material in bigger depth. One can start seeing a noticeable heterogeneity. The same figure also shows the results of the distribution of elements of the same area obtained by means Energy-Dispersive Spectroscopy (EDS) X-ray analysis. The spatial resolution of this mapping is estimated as 2.4 microns using the Anderson - Hasler range [55]. This is a sufficient depth to judge about homogeneity when probing with the nanoindenter and AFM techniques.

One can see a quite homogeneous distribution of the elements like oxygen and carbon. The distributions of silicon and aluminum, which represent silicon dioxide and feldspar, respectively, are more heterogeneous. The distribution of carbon is more important for understanding the mechanical homogeneity of the sample at that scale. This is because the distribution of carbon is indicative of the distribution of the softest organic phase of the shale sample. The softest phase is the biggest contributor to the mechanical response of the composite material. Thus, this indirectly confirms the mechanical heterogeneity of the shale sample at a multi-micron scale.

It should be noted that it is quite challenging to map carbon using EDS technique. Specifically, we have an average of 0.9% of the carbon content with the error of definition of 0.7% (see table S1 for detail). Nevertheless, the certainty percentage of the identification of carbon seems to be quite high (99.3%). Because the goal of this image is to demonstrate the relative homogeneity of the distribution of the organic phase/carbon in a semi-qualitative manner, we consider this accuracy as sufficient.

To add to the proof of the homogeneous distribution of carbon (organic phase, bitumen) near the surface of the shale sample, we analyzed the sample by means of Raman microscopy. The Raman spectrum of the organic phase (bitumen) is shown in Fig.S3 of the Supplementary materials. It has two characteristic peaks known as G and D bands [56]. The origin of the G band (1600 cm^{-1}) is in the E_{2g2} vibrational modes of the carbon atoms in aromatic ring structures (sp^2 carbon) exhibiting D_{6h}^4 symmetry [57]. The D band with a peak at ~1350 cm^{-1} is a result of the Raman-active A_{1g} symmetry associated with lattice defects and discontinuities of the sp_2 carbon network [57]. 1600 cm^{-1} peak is used to map the distribution of the organic phase. Fig.S3b shows the average distribution of depth profile the carbon (bitumen) Raman signal (at 1600 cm^{-1}) obtained on the surface of bitumen and shale, respectively (the averaging was done along a line shown in Fig.S4). Fig. S4 shows the spatial distribution of 1600 cm^{-1} carbon signal across the surface of the sample of bitumen (Fig. S4a) and shale (Fig. S4b). Fig. S4c,d demonstrate the depth dependence 1600 cm^{-1} signal on the bitumen and shale samples, respectively. The decrease of the observed signal decreases with depth because of light absorbance.

Thus, the Raman analysis also shows a rather homogeneous distribution of the organic phase in the shale sample, including the depth distribution up to several microns (Fig. S3b). The absolute value of the Raman intensity indicates a bit lower carbon content of the shale sample compared to bitumen (the imaging of both samples was done by using the same laser intensity). Because the depth decay of the carbon signal in the shale sample is very similar to the one of the bitumen sample (Fig. S3b), one can make a qualitative statement that the organic phase is homogeneously distributed at least several microns in depth from the surface of study. Thus, the Raman microscopy data also indirectly indicates the homogeneous average distribution of the mechanical properties of the shale sample.

Now we can use multiple areas of the shale sample to study the dependence of the obtained modulus on the unload rates. Such dependence is expected because of the presence of the viscoelastic organic phase. The benchmark, the nanoindenter method was used to measure the modulus for four different unloading times, including 1s, 2s, 5s and 10s (the unload speeds are ~1000 nm/s, 500 nm/s, 200 nm/s, and 100 nm/s, respectively). As was mentioned, the PeakForce QNM cannot be used for the measurements with such a low unload rate. The force volume method was used to bridge between the nanoindentation and AFM PeakForce QNM measurements. The unload rates ranging from 200 to 117000 nm/s were used.

The values of the Young's modulus obtained for the shale sample at the different unload rates are summarized in Fig. 7 for all three indentation methods analyzed in this work. The obtained effective Young's modulus obviously depends on the speed of indentation. This dependence becomes apparent only for relatively large speeds, see Table 1 for details. The parameters of the measurements, the number of measured areas, etc. are also shown in Table 1. One can see that the values obtained by all three techniques are in excellent agreement with each other. It is noticeable that the standard deviation is much smaller for the measurements obtained with the nanoindenter approach because each indent has an area of about 4000 times larger than the one obtained with the AFM methods (Table 1). Thus, each nanoindenter measurement is effectively an average of a large number of AFM indentations.

It is also important to note that each AFM measurement cannot be representative of the entire nanocomposite sample, because of at least a very small indentation depth. Nevertheless, multiple measurements at different points of the sample surface are representative because the surface represents a cross-section of the sample bulk. As we see here, it is equivalent to a much smaller number of deeper indentations by the nanoindenter. It is important, though, to verify that we are in the linear stress-strain regime. The latter was verified here by the independence of the modulus of the indentation depth.

It should be noted that we used the unload rate in nm/s, which is obviously just an estimation because the unload rate is hard to control precisely for both the nanoindenter and AFM techniques. The feedback systems of both techniques are based on controlling the force. Furthermore, the AFM feedback is based on the control of just the maximum load force. Thus, the change of indentation is rather nonlinear during unloading. Therefore, the unload rate was calculated using the linear approximation between the initial and final points of indentations. Such approximation results in just a small shift of the data points along the horizontal axis in figure 7. One can see that this approximation is justified by a very weak dependence of the modulus on the indentation rate.

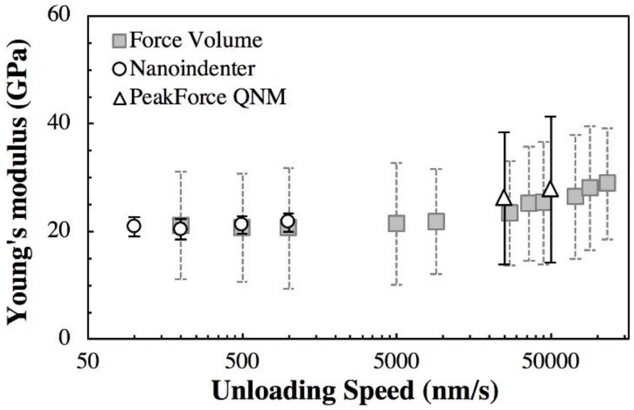

Fig. 6. A summary plot showing the values of the modulus of the shale sample for a range of indentation rates measured by three techniques described in this work: nanoindenter, AFM Force-volume, and AFM PeakForce QNM modes. The mean values of the Young's modulus with one standard deviation (shown as the error bar) are shown for the distribution of 15 × 15 indents for nanoindenter, 32 × 32 indents for force-volume and 128 ×128 indents for PeakForce QNM (high height gradient points were removed). Various unloading speeds were utilized: nanoindenter (the unloading speed of 100 nm/s to 1000 nm/s, applied force 20 mN, indentation depth ~1000 nm), AFM Force-volume (unloading speeds varying from 200 nm/s to 100,000 nm/s; applied force 8 μN; indentation depth ~5 nm) and AFM PeakForce QNM (unloading speeds ~25,000 and 50,000 nm/s; applied force 8 μN; indentation depth ~5 nm).

When comparing the results obtained with the PeakForce QNM and force volume, one can see that the average values of the moduli are not that perfect match as the results with the nanoindenter and force-volume modes. Let us discuss a possible reason for this small (compared to the standard deviation) but still not a symbol difference. As one can see from Table 1, the average (mean) values of the modulus obtained with the PeakForce QNM are larger than the values obtained with the force-volume mode by ~10%. But it is the opposite trend when we compare the mode value (the most probable value of the modulus) ~-8%. We can think about two possible reasons for this small discrepancy. First, the definition of the slope, and subsequently, the areas which are used to calculate the modulus, are noticeably different for the PeakForce and force volume modes. This is because the digital resolution is different (128x128 versus 32x32 pixels). Secondly, the force-volume mode is not intended to run in such a high load/unload speeds. The linear load-unload ramp is substantially disturbed due to the inertia of the scanner. However, as one can see, the discrepancy between the moduli observed with PeakForce and force-volume modes is quite small. It is within the range of a typical error of definition of the spring constant of the AFM cantilever (10-20%). Therefore, we consider the obtained results as an indication of very good agreement between results obtained with the PeakForce and force volume modes.

At the end, it is worth comparing the obtained values of the effective Young's modulus with the modulus values measured for other shale rocks (although shale rocks extracted from different deposits may have substantially different mechanical properties). Due to the variability of shales, the mechanical properties of different shale samples vary from ~15 GPa to ~46 GPa [58-61]. For example, even explored from the same place, the moduli of organic-depleted and organic-rich shales can be quite different, being ~68-~72 GPa and ~38-~46 GPa, respectively [62]. In another example, an average modulus of 16 GPa was reported for an applied force of 4.8 mN (indentation depth ~ 0.6-2.5 μm) [54]. It should be stressed that the shale samples of [54] were quite different because it showed multiple peaks in the distribution of the modulus, whereas our nanoindentation results show only one peak (presumably due to a rather homogeneous distribution of the organic phase as explained above). Nevertheless, the observed values of the modulus are definitely within the range reported in the literature.

Conclusions

An organically rich shale rock sample was used to understand if the AFM technique can be used for the measurements of absolute values of the effective Young's modulus of stiff nanocomposite materials. Two different AFM indentation methods, the force-volume and PeakForce QNM modes were used. The nanoindenter technique was used as the control benchmark. The obtained results show an excellent agreement between the different methods despite using substantially different instruments and models. The nanoindenter method was used as instructed in the manual, and the independence of the modulus of the indentation depth was verified to ensure the self-consistency of the used approach. The atomic force microscopy approach required a more sophisticated approach to be self-consistent. A relatively dull probe was used to avoid nonlinearity of stress-strain response. Following the brush model, which allows excluding the unknown influence of the surface roughness, we demonstrated the measurements of the correct value of the modulus (depth-independent value). As expected from higher sample heterogeneity at the nanoscale, the distribution of the effective Young's modulus over the sample surface was broader when measured with a higher resolution AFM approach compared to nanoindenter. We can see that only AFM could visualize the mechanical properties of the soft organic and hard inorganic phases at the nanoscale. The average values of the modulus obtained with the different techniques are virtually the same, thereby demonstrating the agreement between different techniques. The observed effective modulus slightly increases with the increase of the unloading rate, which is also expected for a viscoelastic material.

Table 1. Summary of the three nanoindentation methods used in this work to study the Young’s modulus on shale.

Methods and Parameters											Young's modulus (GPa)			
Method		Probe	Ramp size (Force volume) /Amplitude (QNM) (nm)	Ramp frequency (Hz)	Model	Ave. Contact diameter (nm)	Ave. Depth (nm)	Unloading speed (nm/s)	Image counts	Image resolution (nm)	Mode	Mean	Stand deviation	Median
Nanoindenter		Berkovich probe	/		Oliver-Pharr	~5000	~1000	100	1	1000	20.9	1.8	21.1	21.3
								200	10		20.4	1.9	20.5	20.9
								500	1		21.3	1.6	21.6	22.0
								1000	1		21.7	1.7	21.9	22.2
AFM	Force volume	Dull AFM probe	200	0.5	DMT	~80	~5	200	10	312	21.1	9.9	20.0	18.0
			500	0.5				500	1		20.7	10.1	20.9	20.4
			1000	0.5				1000	1		20.6	11.2	20.3	20.1
			2500	1				5000	1		21.4	11.3	22.2	21.0
			4500	1				9000	1		21.8	9.8	21.1	20.6
			4500	3				27000	1		23.4	9.7	23.1	22.2
			4500	4				36000	1		25.2	10.6	24.5	23.7
			4500	5				45000	1		25.3	11.4	25.1	23.1
			4500	8				72000	1		26.4	11.5	25.8	25.3
			4500	10				90000	1		28.0	11.5	26.9	26.7
			4500	13				117000	1		28.9	10.3	28.6	28.0
	PeakForce QNM		65	/				25000	10	80	26.2	12.3	24.3	19.7
			200					50000	1		27.8	13.5	26.1	22.1

Conflicts of interest

There are no conflicts to declare.

Acknowledgments

I.S. acknowledges partial support of this work from the National Science Foundation (CBET 1428919, CMMI 1435655, CMMI 1937373). Y.H. and P.P. are thankful for the support of this work from the Special Fund for Strategic Priority Research Program of the Chinese Academy of Sciences (XDA14010102) and National Natural Science Foundation of China (grant no. 41802165). Dr. Voylov is acknowledged for taking Raman images and help in preparing the Raman figures.

References

1. W. K. Liu, E. G. Karpov and H. S. Park, *Nano mechanics and materials : theory, multiscale methods and applications*, John Wiley, Chichester, England ; Hoboken, NJ, 2006.
2. A. Aufderhorst-Roberts, D. Baker, R. J. Foster, O. Cayre, J. Mattsson and S. D. Connell, *Nanoscale*, 2018, **10**, 16050-16061.
3. B. R. Neugirg, S. R. Koebley, H. C. Schniepp and A. Fery, *Nanoscale*, 2016, **8**, 8414-8426.
4. S. El-Kirat-Chatel, A. Beaussart, S. P. Vincent, M. A. Flos, P. Hols, P. N. Lipke and Y. F. Dufrene, *Nanoscale*, 2015, **7**, 1760-1767.
5. Y. F. Dufrene and A. E. Pelling, *Nanoscale*, 2013, **5**, 4094-4104.
6. A. Stylianou, M. Lekka and T. Stylianopoulos, *Nanoscale*, 2018, **10**, 20930-20945.
7. S. Suresh, *Acta Biomater*, 2007, **3**, 413-438.
8. S. E. Cross, Y. S. Jin, J. Tondre, R. Wong, J. Rao and J. K. Gimzewski, *Nanotechnology*, 2008, **19**, 384003.
9. I. Sokolov, S. Iyer and C. D. Woodworth, *Nanomed-Nanotechnol*, 2006, **2**, 31-36.
10. T. K. Berdyyeva, C. D. Woodworth and I. Sokolov, *Physics in Medicine and Biology*, 2005, **50**, 81-92.
11. W. C. Oliver and G. M. Pharr, *Journal of Materials Research*, 2004, **19**, 3-20.
12. M. E. Dokukin and I. Sokolov, *Macromolecules*, 2012, **45**, 4277-4288.
13. V. Kumar, M. E. Curtis, N. Gupta, C. H. Sondergeld and C. S. Rai, presented in part at the Society of Petroleum Engineers162778, 2012.
14. A. E. Hassan, W. F. Heinz, M. D. Antonik, N. P. D'Costa, S. Nageswaran, C. A. Schoenenberger and J. H. Hoh, *Biophys J*, 1998, **74**, 1564-1578.
15. J. H. Hoh and C. A. Schoenenberger, *J Cell Sci*, 1994, **107 (Pt 5)**, 1105-1114.
16. M. E. Dokukin and I. Sokolov, *Langmuir*, 2012, **28**, 16060-16071.
17. B. Pittenger, N. Erina and C. Su, 2014, **203**, 31-51.
18. K. Sweers, K. van der Werf, M. Bennink and V. Subramaniam, *Nanoscale research letters*, 2011, **6**, 270.
19. S. Iwamoto, W. Kai, A. Isogai and T. Iwata, *Biomacromolecules*, 2009, **10**, 2571-2576.
20. J. Adamcik, C. Lara, I. Usov, J. S. Jeong, F. S. Ruggeri, G. Dietler, H. A. Lashuel, I. W. Hamley and R. Mezzenga, *Nanoscale*, 2012, **4**, 4426.
21. P. Schön, K. Bagdi, K. Molnár, P. Markus, B. Pukánszky and G. Julius Vancso, *European Polymer Journal*, 2011, **47**, 692-698.
22. M. E. Dokukin and I. Sokolov, *Langmuir : the ACS journal of surfaces and colloids*, 2012, **28**, 16060-16071.
23. P. Trtik, J. Kaufmann and U. Volz, *Cement and Concrete Research*, 2012, **42**, 215-221.
24. S. Emmanuel, M. Eliyahu, R. J. Day-Stirrat, R. Hofmann and C. I. Macaulay, *Marine and Petroleum Geology*, 2016, **70**, 175-184.
25. M. Eliyahu, S. Emmanuel, R. J. Day-Stirrat and C. I. Macaulay, *Marine and Petroleum Geology*, 2015, **59**, 294-304.
26. Y. Liu, Y. Xiong, Y. Li and P. a. Peng, *Marine and Petroleum Geology*, 2018, **92**, 780-793.
27. J. F. W. Gale, S. E. Laubach, J. E. Olson, P. Eichhuble and A. Fall, *AAPG Bulletin*, 2014, **98**, 2165-2216.
28. A. Dahi-Taleghani and J. E. Olson, *SPE-124884-PA*, 2011, **16**, 575-581.
29. R. Z. Zhong, S. Miska and M. J. Yu, *J Nat Gas Sci Eng*, 2017, **38**, 475-484.
30. E. C. Koncagül and P. M. Santi, *International Journal of Rock Mechanics and Mining Sciences*, 1999, **36**, 139-153.
31. L. L. Lacy.
32. L. B. Colmenares and M. D. Zoback, *International Journal of Rock Mechanics and Mining Sciences*, 2002, **39**, 695-729.
33. A. M. Lucier, R. Hofmann and L. T. Bryndzia, *The leading edge*, 2011, **30**, 300-311.
34. M. Tianshou and C. Ping, *Petroleum Exploration and Development*, 2014, **41**, 249-256.
35. H. Wang, Y. Liu, D. Dong, Q. Zhao and D. Du, *Petroleum Exploration and Development*, 2013, **40**, 615-620.
36. M. Shi, B. Yu, Z. Xue, J. Wu and Y. Yuan, *Journal of Natural Gas Science and Engineering*, 2015, **26**, 948-959.
37. M. Wei, L. Zhang, Y. Xiong, J. Li and P. a. Peng, *Microporous and Mesoporous Materials*, 2016, **227**, 88-94.
38. H. Tian, L. Pan, T. Zhang, X. Xiao, Z. Meng and B. Huang, *Marine and Petroleum Geology*, 2015, **62**, 28-43.
39. T. Cao, Z. Song, S. Wang, X. Cao, Y. Li and J. Xia, *Marine and Petroleum Geology*, 2015, **61**, 140-150.
40. D. Liu, X. Xiao, H. Tian, Y. Min, Q. Zhou, P. Cheng and J. Shen, *Chinese Science Bulletin*, 2012, **58**, 1285-1298.
41. W. C. Oliver and G. M. Pharr, *Journal of Materials Research Home*, 1992, **7**, 1564-1583.
42. C. Li, M. Ostadhassan, S. Guo, T. Gentzis and L. Kong, *Fuel*, 2018, **233**, 894-910.
43. *Journal*, 1999, CD-ROMs.
44. J. Hu, W. Sun, Z. Jiang, W. Zhang, J. Lu, W. Huo, Y. Zhang and P. Zhang, *Materials Science and Engineering: A*, 2017, **686**, 19-25.
45. A. A. Elmustafa and D. S. Stone, *Acta Materialia*, 2002, **50**, 3641-3650.
46. P. S. Phani and W. C. Oliver, *Mater Design*, 2019, **164**.
47. P. H. Wu, D. R. B. Aroush, A. Asnacios, W. C. Chen, M. E. Dokukin, B. L. Doss, P. Durand-Smet, A. Ekpenyong, J. Guck, N. V. Guz, P. A. Janmey, J. S. H. Lee, N. M. Moore, A. Ott, Y.

C. Poh, R. Ros, M. Sander, I. Sokolov, J. R. Staunton, N. Wang, G. Whyte and D. Wirtz, *Nature Methods*, 2018, **15**, 491-498.

48. N. Guz, M. Dokukin, V. Kalaparthi and I. Sokolov, *Biophys J*, 2014, **107**, 564-575.

49. P. J. Cumpson, P. Zhdan and J. Hedley, *Ultramicroscopy*, 2004, **100**, 241-251.

50. H. Hertz, D. E. Jones and G. A. Schott, *Miscellaneous papers*, Macmillan and Company, 1896.

51. I. Sokolov and M. E. Dokukin, *Nanoscale Imaging: Methods and Protocols*, 2018, **1814**, 449-468.

52. M. E. Dokukin, H. Kuroki, S. Minko and I. Sokolov, *Macromolecules*, 2017, **50**, 275-282.

53. I. Sokolov, M. E. Dokukin and N. V. Guz, *Methods*, 2013, **60**, 202-213.

54. C. Bobko and F.-J. Ulm, *Mechanics of Materials*, 2008, **40**, 318-337.

55. J. Goldstein, *Scanning electron microscopy and x-ray microanalysis*, Springer Science+Business Media, LLC, New York, NY, 4th edition. edn., 2017.

56. S. Khatibi, M. Ostadhassan, D. Tuschel, T. Gentzis, B. Bubach and H. Carvajal-Ortiz, *International Journal of Coal Geology*, 2018, **185**, 103-118.

57. B. Sauerer, P. R. Craddock, M. D. AlJohani, K. L. Alsamadony and W. Abdallah, *International Journal of Coal Geology*, 2017, **173**, 150-157.

58. M. Fan, Y. Jin, M. Chen and Z. Geng, *Journal of Petroleum Science and Engineering*, 2019, **174**, 607-616.

59. K. Liu, M. Ostadhassan, B. Bubach, K. Ling, B. Tokhmechi and D. Robert, *Journal of Natural Gas Science & Engineering*, 2018, **53**, S1875510018301203.

60. C. Li, M. Ostadhassan, A. Abarghani, A. Fogden and L. Kong, *Journal of Materials Science*, 2018, **54**, 2133-2151.

61. Y. B. Veytskin, V. K. Tammina, C. P. Bobko, P. G. Hartley, M. B. Clennell, D. N. Dewhurst and R. R. Dagastine, *Geomechanics for Energy and the Environment*, 2017, **9**, 21-35.

62. M. Mashhadian, A. Verde, P. Sharma and S. Abedi, *Journal of Petroleum Science and Engineering*, 2018, **165**, 313-324.